

PAPER

Polytypism in ultrathin tellurium

To cite this article: Amey Apte *et al* 2019 *2D Mater.* **6** 015013

View the [article online](#) for updates and enhancements.



IOP | ebooksTM

Bringing you innovative digital publishing with leading voices to create your essential collection of books in STEM research.

Start exploring the collection - download the first chapter of every title for free.



PAPER

Polytypism in ultrathin tellurium

RECEIVED
2 August 2018REVISED
26 September 2018ACCEPTED FOR PUBLICATION
12 October 2018PUBLISHED
12 November 2018

Amey Apte^{1,9}, Elisabeth Bianco^{3,9}, Aravind Krishnamoorthy^{3,9}, Sadegh Yazdi¹, Rahul Rao⁴, Nicholas Glavin⁴, Hiroyuki Kumazoe⁵, Vikas Varshney⁴, Ajit Roy⁴, Fuyuki Shimojo⁵, Emilie Ringe^{1,2,6,7}, Rajiv K Kalia³, Aiichiro Nakano³, Chandra Sekhar Tiwary^{1,8,10}, Priya Vashishta^{3,10}, Vidya Kochat^{1,10} and Pulickel M Ajayan^{1,10}

- ¹ Department of Materials Science and NanoEngineering, Rice University, 6100 Main St, Houston, TX 77005, United States of America
² Department of Chemistry, Rice University, 6100 Main St, Houston, TX 77005, United States of America
³ Collaboratory for Advanced Computing and Simulations, University of Southern California, 3651 Watt Way, VHE 610, Los Angeles, CA 90089-0242, United States of America
⁴ Materials and Manufacturing Directorate Air Force Research Laboratory, WPAFB, OH 45433, United States of America
⁵ Department of Physics, Kumamoto University, Kumamoto 860-8555, Japan
⁶ Department of Materials Science and Metallurgy, University of Cambridge, 27 Charles Babbage Road, Cambridge CB3 0FS, United Kingdom
⁷ Department of Earth Sciences, University of Cambridge, Downing Street, Cambridge CB2 3EQ, United Kingdom
⁸ Metallurgical and Materials Engineering, Indian Institute of Technology, Kharagpur, 721302, West Bengal, India
⁹ These authors contributed equally to the work.
¹⁰ Authors to whom any correspondence should be addressed.

E-mail: cst.iisc@gmail.com, priyav@usc.edu, vidyakochat@gmail.com and ajayan@rice.edu

Keywords: 2d materials, tellurene, synthesis, polytypism

Supplementary material for this article is available [online](#)

Abstract

We report the synthesis of ultrathin tellurium films, including atomically thin tellurium tri-layers, by physical vapor deposition (PVD) as well as larger area films by pulsed laser deposition (PLD). PVD leads to sub-nanometer, tri-layer tellurene flakes with distinct boundaries, whereas PLD yields uniform and contiguous sub-7 nm films over a centimeter square. The PLD films exhibit the characteristic hexagonal crystal structure of semiconducting tellurium, but high resolution transmission electron microscopy (HRTEM) reveals a unique stacking polytype in the thinner PVD-grown material. Density Functional Theory calculations predict the possible existence of three polytypes of ultrathin Te, including the α -type experimentally observed here. The two complementary growth methods afford a route to controllably synthesize ultrathin Te with thicknesses ranging from three atomic layers up to 6 nm with unique polytypism. Lastly, temperature dependent Raman studies suggest the possible coexistence of polymorphs.

1. Introduction

Layered materials have gained widespread attention from the 2D community following the isolation of graphene and exploration of its multitude of unique properties; since then, 2D materials such as transition metal dichalcogenides, layered high T_c superconductors, and elemental 2D materials synonymous to graphene such as silicene, germanene, stanene, phosphorene and borophene have been experimentally realized [1–14]. These 2D materials have enabled the realization of high performance field effect transistors (FETs) operating at room temperature with applications envisaged in the fields of optoelectronics, energy storage, and sensors [1, 15–17]. The massless Dirac fermionic nature of

charge carriers, first visualized in graphene in the form of the half-integer quantum Hall effect, has now been proposed to exist in its elemental analogues such as silicene and germanene, having buckled honeycomb lattices [1, 16, 17]. Stanene, contrary to graphene, has strong spin-orbit coupling giving rise to a sizeable bandgap (0.3 eV) and is predicted to be a 2D topological insulator with dissipationless electrical conduction at even room temperatures due to topologically protected edge states [12, 18]. Phosphorene has emerged as a strong competitor for graphene due to the presence of a bandgap of 1.88 eV in the monolayer case, an on/off ratio of $\sim 10^5$, and field effect hole mobility of $\sim 1000 \text{ cm}^2 \text{ V}^{-1} \text{ s}^{-1}$ observed in few layer FETs [13, 19–21]. On the other hand, borophene, a recent inclusion to the elemental 2D

family, exhibits metallic behavior characteristic of a highly anisotropic 2D metal [11, 22]. Stable 2D layers of Group VI elements offer interesting prospects with the one of the most likely candidates being Tellurium (Te) owing to its unusual anisotropic crystal structure and high melting point of ~ 450 °C [23, 24].

Even in bulk, Te exists as a pseudo-low dimensional form of 1D helical chains of covalently bonded atoms running parallel to the *c*-axis, where these chains are bound via weak van der Waals forces in a hexagonal lattice with $P3_121$ space group symmetry [25, 26]. Bulk Te is a p-type semiconductor with a band gap of 0.34 eV and has attractive properties such as photoconductivity, non-linear optical response, and thermoelectric and piezoelectric behavior [27–31]. This warrants interest in the structural evaluation and synthesis of 2D Te films (monolayers of which is termed tellurene) that could demonstrate new applications for 2D materials. Basic physical properties, such as atomic radius, atomic number and mass of Te, are greater than all other elemental 2D materials (C, B, Sn, Si and P) which also make it more interesting. It also has the highest melting point (449.5 °C) of group VI (compared to 239.4 and 429.5 °C for S and Se respectively). Recent theoretical efforts also show an abnormally low thermal conductivity for 2D Te which opens up potential applications in thermoelectric devices [32]. These points have made tellurene interesting in comparison to other 2D materials. This has motivated several recent theoretical investigations in low-dimensional tellurium crystal structures, which have identified multiple 2D polymorphs of tellurium that are approximately 0.2 eV/Te atom more metastable than bulk Te, suggesting that these crystals can be experimentally realized [33–36]. The α -polytype is predicted to show electron and hole mobilities three orders of magnitude superior to monolayer MoS₂ as well as good optical absorption [37]. Moreover, structural anisotropy is expected to manifest in these properties which will make such tellurene polytypes good candidates for optoelectronics applications. However, in order to reach that stage, it is necessary to understand and develop reproducible synthetic methods. Progress in growth of lateral Te structures was made by Wang *et al* via synthesis of ~ 30 nm thick Te nano-plates on mica for optoelectronic applications [23]. Peide Ye's group has reported studies of strain-dependent Raman spectra and electrical transport properties of 2D Te synthesized via solution-based methods [38, 39]. Thinner Te samples (~ 0.39 nm) were obtained by Huang *et al* via molecular beam epitaxy on graphene/6H-SiC (0001) substrates for studying the band edge structure via scanning tunneling spectroscopy [40]. However, this work was all performed under ultra-high vacuum conditions and did not investigate stability under ambient conditions.

In this work, we demonstrate two simple routes toward ultrathin Te, both yielding sub-7 nm thickness and 50 micron flakes as thin as three atomic layers: first,

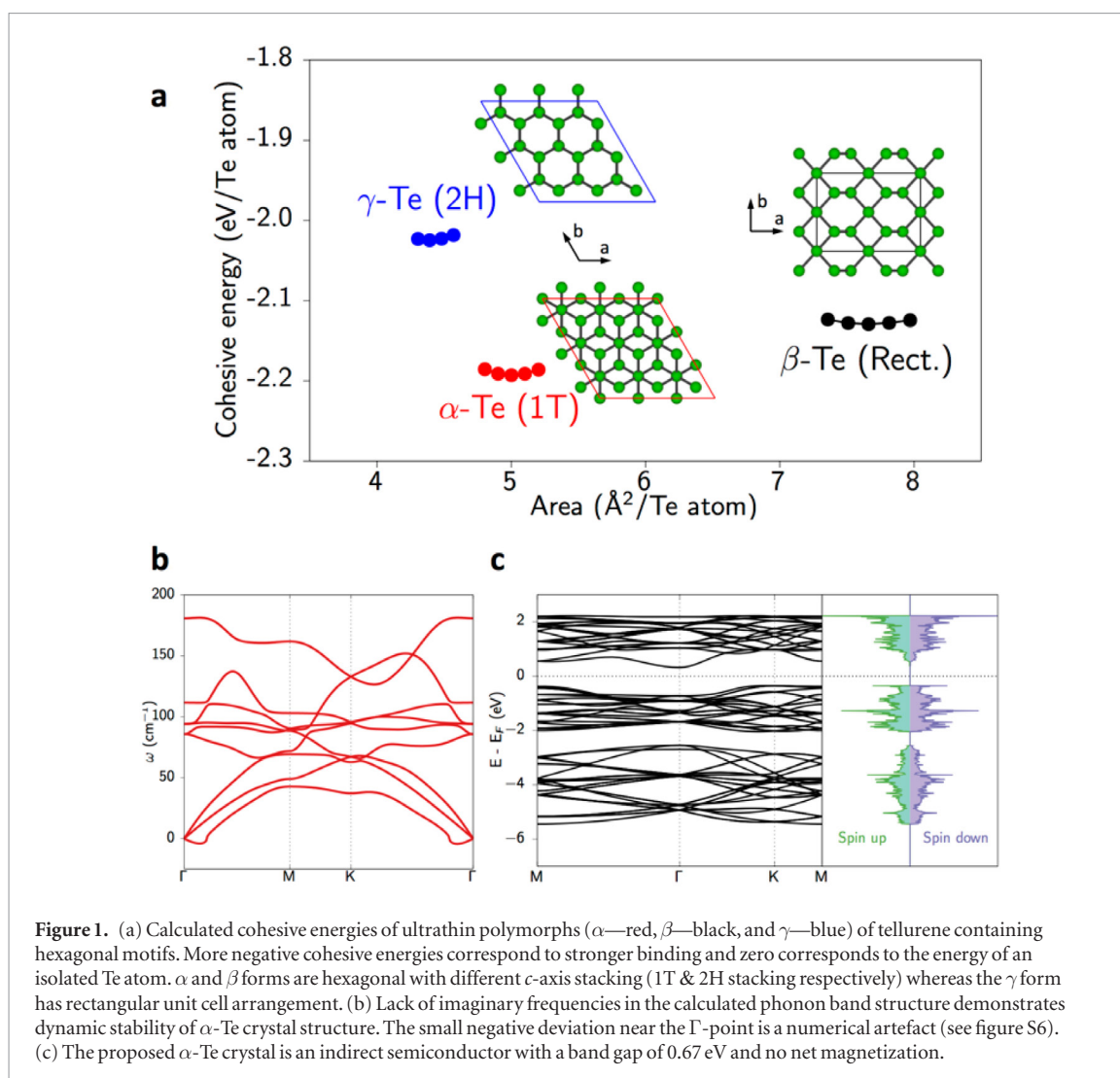
a facile and relatively inexpensive experimental growth of 1–3 layer tellurene films (~ 0.85 nm) using physical vapor deposition (PVD) from bulk Te powder on Si/SiO₂ substrates, and second, 2.7–6.0 nm thick films covering 1 cm² area by pulsed laser deposition (PLD) on MgO substrates. The observed structure(s) of the PVD-grown ultrathin Te were compared with theoretically predicted structures. The theoretical electronic properties were studied using quantum molecular dynamics simulations and density functional theory calculations. To elucidate the structure, we use density functional theory to estimate the relative stabilities and dynamic stability of three previously investigated layered Te crystal structures. Simulation parameters are described in the simulation detail section in the supplemental information.

2. Results and discussion

Figure 1 shows the different possible polytypes for ultrathin Te, with the α -Te crystal polytype, which is akin to the 1T crystal symmetry of transition metal dichalcogenides, being the most stable (0.05 eV/atom and 0.15 eV/atom more energetically stable than the β - and γ phases respectively). This is consistent with previous computational reports of the relative stability of the α crystal structure [37]. Figure 1 also demonstrates that both the ground state α phase and the metastable β and γ phases are dynamically stable relative to biaxial tension and compression. Supplementary tables S1 (stacks.iop.org/TDM/6/015013/mmedia) and S2 list the optimized lattice parameters and atomic positions, respectively, whereas supplementary table S3 lists the Te–Te bond lengths and Te–Te–Te bond angles.

2.1. Pulsed laser deposition

A fundamental challenge for unique, single-element 2D materials is achieving reproducible and scalable large-area growths. Accordingly, we also demonstrate PLD as an alternative growth route to overcome these challenges. Te films ranging 2.7–6 nm in thickness were grown via PLD on 1 cm \times 1 cm single crystal MgO (100). Film growth yields complete substrate coverage and thickness can be varied controllably and reproducibly by varying the number of pulses, which is confirmed by Raman spectroscopy and AFM (figures 2(b) and (c)). The high surface energy of Te results in a strong propensity toward the formation of droplets or islands on a surface during thin film growth, which has historically precluded the coalescence of continuous films thinner than 30 nm [41]. The preclusion of a uniform, continuous layer thinner than 30 nm is explained by the Te crystal structure. The strong covalent bonding along the *c*-axis as compared to the *a*-axis results in surface free energy up to three times higher for the {0001} planes (basal plane during growth) than any other family of planes in the system [42]. This tendency is not inhibitory when growing thick films but poses a substantial challenge for



achieving ultrathin materials. The high vapor pressure of tellurium further compounds this challenge by restricting deposition to low temperature ($<150^\circ\text{C}$) in vacuum [43, 44]. Due to the large kinetic energy of the atomic and ionized species in the plasma plume, PLD affords a route to island breakup, providing an advantage over other, thermodynamically driven high-vacuum deposition techniques, such as molecular beam epitaxy, in depositing ultrathin chalcogen films. Here, a 248 nm KrF laser was focused on a Te target positioned 3 cm from the substrate as shown in figure 2(a). MgO is a common PLD substrate because it is inexpensive and offers high chemical stability, which is especially important during the deposition of chalcogen films due to their reactivity. Deposition was performed at 25°C and chamber base pressure of 10^{-8} torr. The film thickness can be controlled by varying number of pulses (2–8) at a constant fluence of 18.0 J cm^{-2} and 1 Hz repetition rate.

The Te films deposited via PLD on MgO (100) are contiguous, leading to complete substrate coverage, and appear flat under optical microscopy (figure S8(a)). The contrast between the substrate and Te film is evident in the lower left region of the image where a strip of photoresist has been removed. Thickness of

the PLD-grown samples was measured across a step-edge created by masking a portion of the substrate with a thin photoresist (figure 2(b)). These films were found to be 2.7, 3.9, and 6 nm thick, for samples grown using 2, 4, and 8 laser pulses, respectively. Cross-sectional high resolution TEM (HRTEM) images of the eight pulse PLD-grown sample prepared by low-angle Ar^+ ion milling show thickness of $\sim 6\text{ nm}$ (figures 2(d) and (e)), in agreement with the thickness measured by AFM. The crystal structure observed in the HRTEM is consistent with that of hexagonal, $P3_121$ structure, and the lowest index diffraction spots in the fast Fourier transform (FFT) have d -spacings of 3.24 \AA (yellow circle) and 2.22 \AA (blue circle) respectively (figure 2(d), inset)). The same two diffraction spots are observed in the SAED pattern (figure S12) which, despite the square appearance of the FFT, are attributed to the hexagonal crystal structure as viewed down this particular zone axis. While the precise zone axis cannot be determined without a second orientation, precluding indexing of the diffraction spots, the image is concluded to be taken from either the $[1\ -101]$, $[12\ -31]$, or $[21\ -3\ -1]$ zone axis, as all three have diffraction patterns with reflections of equivalent d -spacing (figure S14). To support this, figure 3(e)

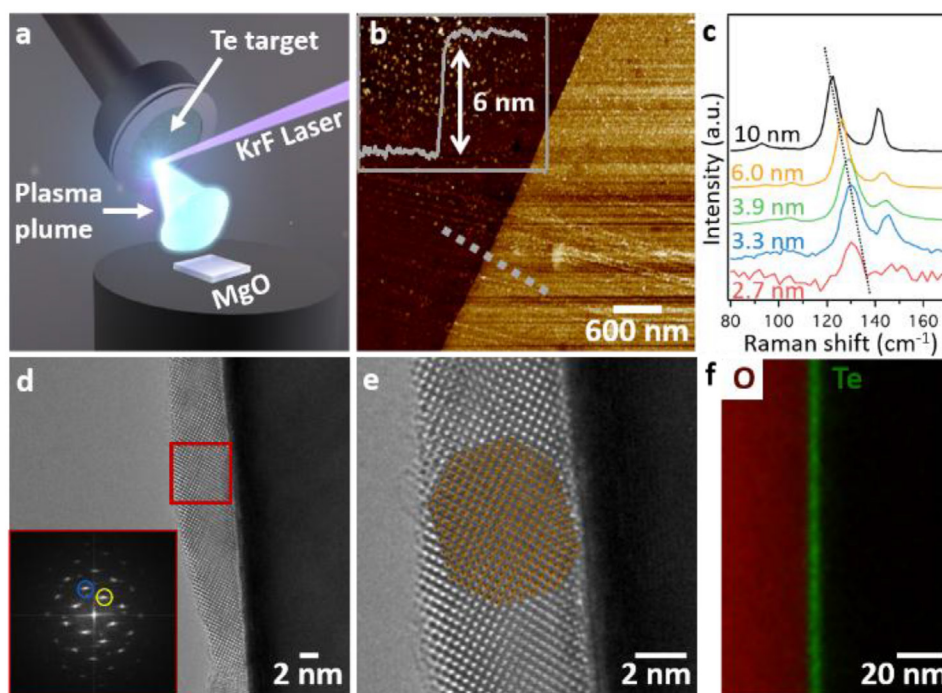


Figure 2. (a) Schematic of the PLD setup. (b) AFM micrograph and height profile (inset) of an 8-pulse PLD film. (c) Raman spectra of films of varying thicknesses. The black dotted line demonstrates the systematic blue shift of the A_1 mode as thickness decreases. (d) Cross-sectional HRTEM/FFT (inset) and (e) HRTEM images of a 6 nm Te film on MgO (100). Blue and yellow circles correspond to d-spacings of 2.22 Å and 3.24 Å respectively (figure S12). (f) Corresponding EDS map of the Te $L\alpha$ and O $K\alpha$ peaks shows the abrupt substrate/film interface.

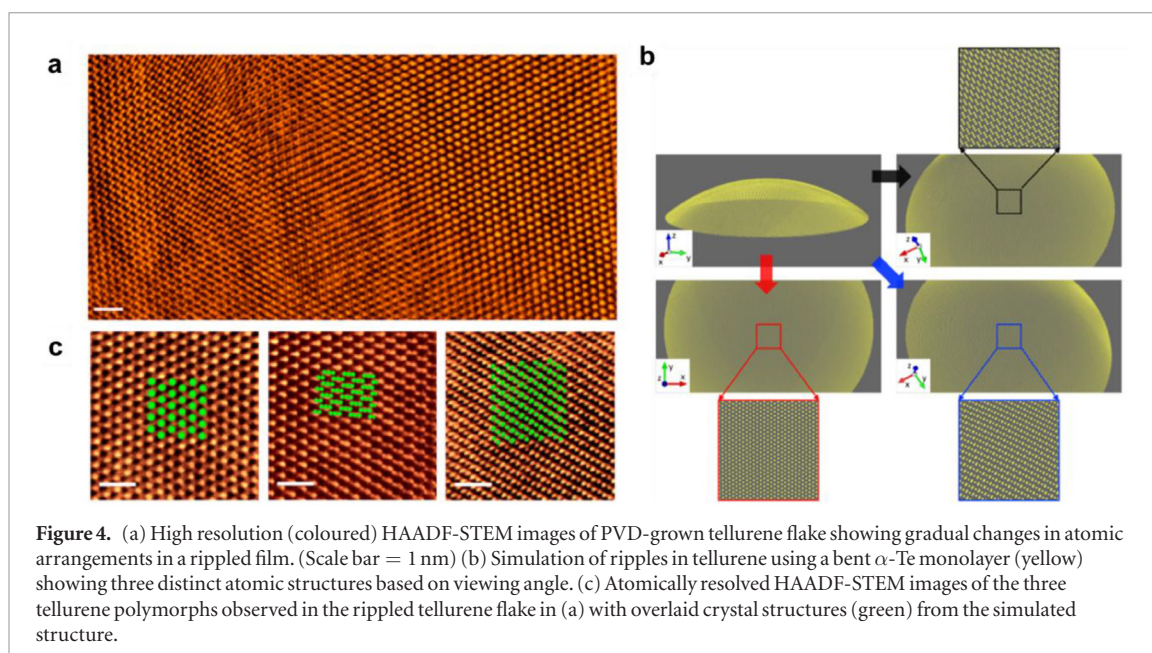
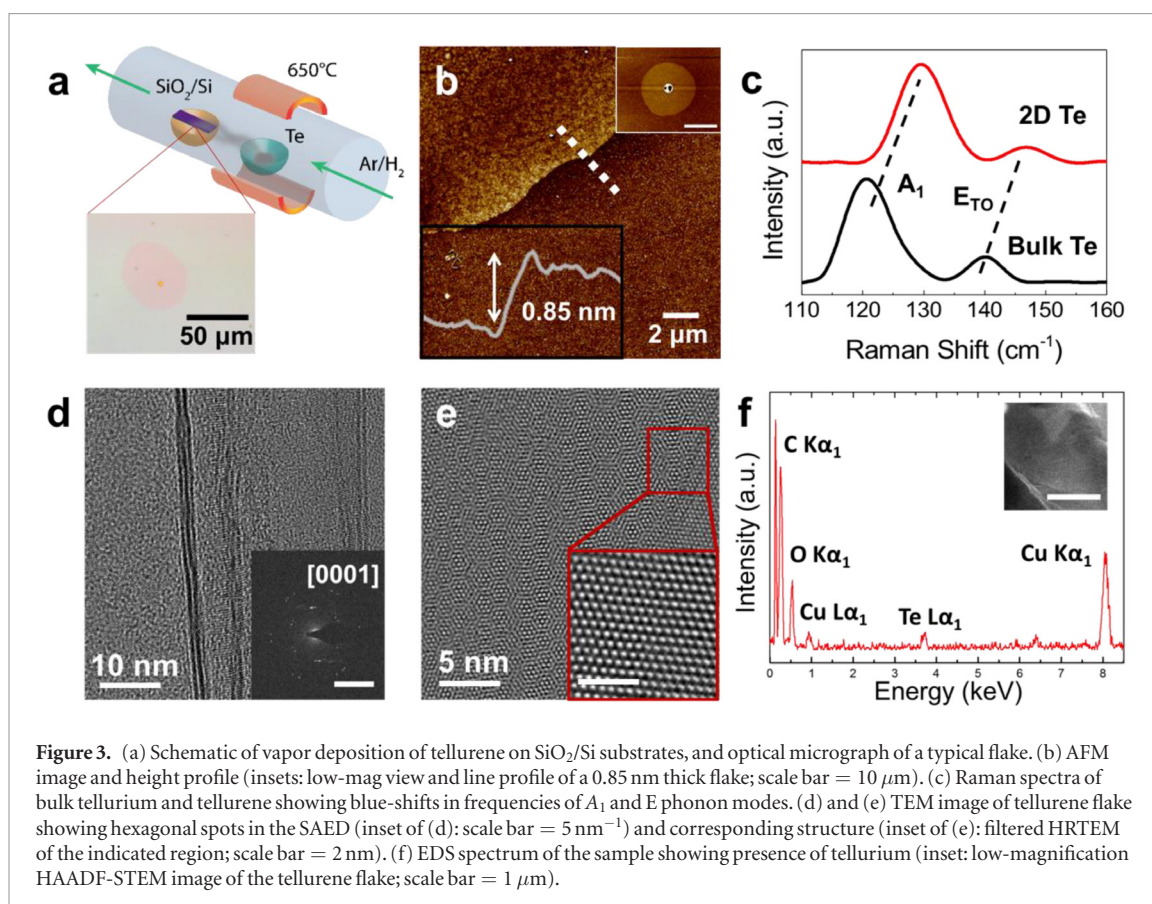
shows the Te lattice viewed down the $[1 -1 0 1]$ zone axis and overlaid onto the HRTEM image, which is the most likely zone axis due to the 45° off-axis deposition geometry. The registry between the two confirms that the crystal structure is indeed consistent with that of $P3121$ Te. EDS maps do not reveal the existence of oxidation in the film, as O signal correlates with that of Mg from the substrate and drops off sharply at the Te/MgO interface (figure 2(f)). Furthermore, an EDS line profile across the interface shows the same trend with both O and Mg signal dropping off at the MgO/Te interface. From this, we conclude that the PLD-grown Te films are not subject to oxidation. Thus, we show that PVD synthesis enables a highly facile and fast route to obtain high-quality and ultrathin tellurium flakes whereas PLD results in slightly thicker (yet sub-7 nm) but highly uniform and contiguous tellurium films. Both films exhibit hexagonal, $P3_121$ structure with similar Raman modes, however, as will be discussed in the next section, the PVD-grown material exhibits a unique stacking polytype. Furthermore, STEM-EDS shows little to no oxide coexistence.

2.2. Physical vapor deposition

The thermal evaporation of bulk Te in an Ar/H₂ atmosphere at a temperature of 650 °C results in the growth of ultrathin films on Si/SiO₂ substrates, with lateral sizes varying from 10 to 100 μm (figure 3(a)). The atomic force microscopy (AFM) image in figure 3(b) reveals uniform atomically thin films of thickness 0.85 ± 0.1 nm. Considering the Te–Te

bond length of hexagonal tellurium (2.86 Å) and the interatomic layer separation (3.67 Å), this corresponds to three atomic layers [37, 45]. Figures 3(d) and (e) show transmission electron microscopy (TEM) images of a large (~10 μm), atomically thin flake. The selected-area electron diffraction (SAED) pattern confirms the hexagonal symmetry with three distinct sets of six-fold diffraction spots. The three sets of spots are indicative of turbostratic disorder between 3 layers, consistent with observed Moiré interference patterns (figures 3(e) and S7). The energy-dispersive x-ray spectrum (EDS) obtained from such a flake is shown in figure 3(f) with clear indication of the presence of Te. The inset shows a low magnification STEM image of this flake.

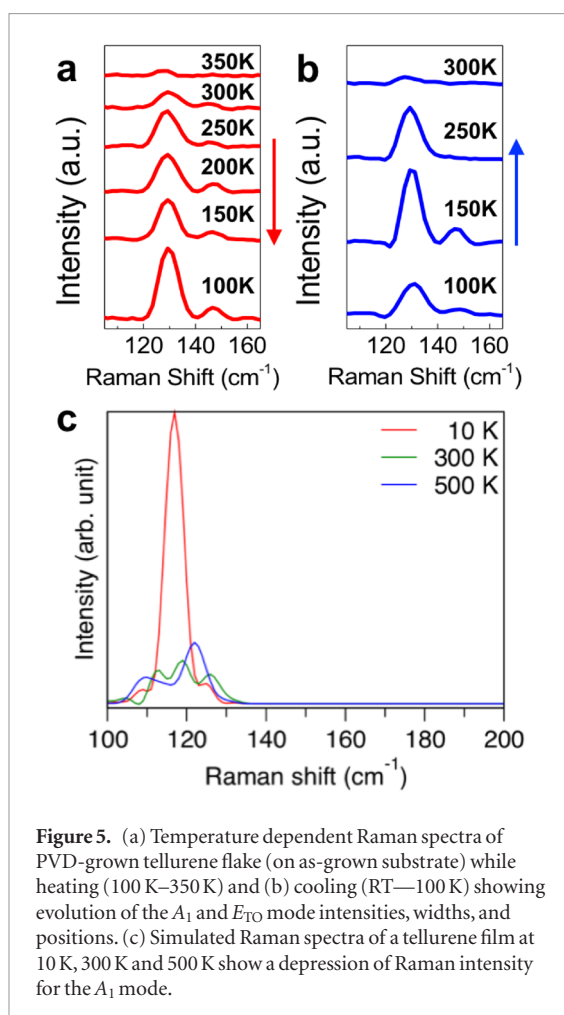
High resolution STEM imaging of the PVD-grown ultrathin Te films displayed in figure 4(a) reveals the existence of the α -polytype in this material. Furthermore, the lattice structure seemingly varies from left to right. Under initial inspection, it appears that all three predicted polytypes, α , β , and γ , exist. This, however, is not the case, and complementary images, diffraction, and simulations reveal the existence of only the α polytype. The apparent change in crystalline structure is attributed to rippling of the Te film. Despite the fact that the lattice arrangement looks very different in different regions of figure 4(a), in the SAED shown in figure 3(d) shows a single crystalline phase. Additionally, no sharp boundaries or interfaces are observable in the STEM images. Rather gradual changes consistent with bending are observed. Formation of similar



ripples have been observed in freestanding graphene and MoS₂ using aberration-corrected STEM [46–48]. To confirm this, we compare three distinct atomic arrangements (figure 4(b)) found in the HAADF-STEM image with atomic configurations found in a simulated ripple constructed from a monolayer of the ideal α -Te crystal bent with a radius of curvature of 400 Å. The appearance of the Te film in simulated images is consistent with what is observed in the real image—the α -Te structure is consistent with the expected appearance in flat regions as well as in rippled regions

where the lattice appears distorted. This pronounced rippling is supported by the low value of calculated elastic moduli (44.5 Nm⁻¹) in comparison to other monolayer materials (180 Nm⁻¹ MoSe₂ and 340 Nm⁻¹ for graphene) and comparable to other elemental 2D materials (~70 Nm⁻¹ for silicene and 29–52 Nm⁻¹ for black phosphorus) [49–52].

Temperature and thickness dependent Raman spectroscopy was used to further explore the lattice of PVD-grown and PLD-grown films, as well as bulk Te. The Raman modes at 121.5 cm⁻¹ and 140.8 cm⁻¹ in



bulk Te correspond to modes with A_1 and E symmetry respectively. The A_1 mode arises from vibrations in the basal plane and the E_{TO} mode arises from asymmetric bond-stretching along c -axis [23, 53]. As the thickness decreases from bulk Te to 2D, these modes blue shift to $\sim 129 \text{ cm}^{-1}$ and 146 cm^{-1} respectively as shown in figures 2(c) and 5(a), which can be attributed to the reduced long-range Coulombic interlayer interactions in tri-layer tellurene. Similarly, a systematic blue shift of the A_1 and E modes is observed in the PLD-deposited films as the thickness is reduced from 6 nm to 2.7 nm (figure 3(c), S11). The peak position transitions in a near-linear fashion from 126 cm^{-1} to 128 cm^{-1} . This could suggest the orientation of the films having the c -axis orthogonal to the substrate surface. In both PLD and PVD samples, no peaks arising from tellurium oxide are observed. Figure 5(a) shows the temperature dependent evolution of the Raman modes in tri-layer tellurene. With increase in temperature from 100 K to 350 K, a sharp decrease in the intensities of the peaks is observed. This decrease in intensities is supported by simulated Raman spectra (figure 5(b)) obtained from quantum molecular dynamics trajectories obtained at low and high temperatures [54]. While the peaks are distinct at low temperatures, they undergo significant broadening as temperature is increased. Upon cooling, the structure of the peaks is regained suggesting a reversible improvement in crystallinity. Both the

Raman modes A_1 and E_{TO} red shift with increase in temperature, whose frequency shifts can be fitted with the following relation [55]:

$$\omega = \omega_0 + \chi T.$$

Where ω is the frequency of the Raman modes at 0 K and χ is the first order temperature coefficient of these modes from which we extract the values $\chi_{A_1} = (-3.6 \pm 0.6) \times 10^{-3} \text{ cm}^{-1} \text{ K}^{-1}$ and $\chi_{E_{TO}} = (-5.1 \pm 0.8) \times 10^{-3} \text{ cm}^{-1} \text{ K}^{-1}$. The temperature dependence of the phonon frequency results from the thermal expansion and anharmonic contribution causing a self-energy shift at higher temperatures [56]. The HAADF-STEM images of tri-layer tellurene at 300 K reveal the plausible reason for the broadening and weakening of Raman modes observed at high temperature. One reason could be the co-existence of various stable polymorphic structures at higher temperatures (300 K and above) as shown in figures 4(a) and (c). These polymorphic regions spanning a few nm in size can result in lattice strain at the boundaries leading to significant contortions which affect the intensity of the Raman modes. As the temperature is lowered, the strain relaxation can affect the movement of atoms in the basal planes more than the out-of-plane vibrations for the ultrathin morphologies; as a result, the Raman intensity of the A_1 mode of tellurene is affected to a greater degree than that of the E_{TO} mode as a function of temperature, as seen from figure 5(a). This can also mean that such a disproportionate effect is more pronounced in the few-layer PVD-grown sample as compared to the thicker PLD-grown counterpart.

3. Conclusions

We demonstrate growth of ultrathin tellurene films via two complimentary routes: PVD and PLD. The former presents a facile, rapid, and relatively inexpensive route to obtaining among the thinnest 2D tellurium crystals reported to date exhibiting a unique polytype from bulk Te, whereas the latter route enables uniform and contiguous and scalable growth of sub-7 nm ultrathin Te films of controllable thickness at room temperature. HAADF-STEM imaging of the PVD-grown tri-layer tellurene flake shows different atomic arrangements within the same sample, which is attributed to rippling of the suspended α -Te film, which is dynamically stable, but has low stiffness. The temperature dependent Raman spectra of PVD-grown tellurene show shifts due to lattice expansion coefficients and anharmonic behavior which is correlated with the possible coexistence of the multiple polymorphs and the resulting strain at the nm-sized boundaries.

4. Experimental details

4.1. Pulsed laser deposition (PLD)

PLD-deposited films were grown on epi-ready single crystal MgO (100) (MTI Corporation). Prior

to loading into the vacuum chamber, the MgO was sonicated in acetone (Fisher Chemical, semiconductor grade) and isopropanol (Fisher Chemical, semiconductor grade). A Lambda-Physik LPX300 KrF laser (248 nm) was focused to a spot size of $2.6 \text{ mm} \times 1.5 \text{ mm}$ onto a 1" Te target (Kurt J Lesker, 99.999%) at a working distance of 3 cm. ten pulses at a fluence of 18.0 J cm^{-2} and 1 Hz repetition rate were used. Films were grown at $25 \text{ }^\circ\text{C}$ and chamber base pressure (10^{-8} torr). To measure film thickness via AFM, a thin strip of photoresist was used to cover a portion of the substrate during deposition and subsequently removed, yielding a measurable step-edge.

4.2. Physical vapor deposition

PVD tellurene was grown in a 2" quartz tube furnace with 10 mg tellurium (Sigma Aldrich, 99.99%) powder in a porcelain boat and a long SiO_2/Si substrate (300 nm oxide layer, pre-cleaned with acetone and isopropanol) positioned 6 cm downstream. The temperature at the Te source was ramped up to $650 \text{ }^\circ\text{C}$ in 23 min and held for 8 min followed by ambient cooling. 100 sccm Ar/H_2 (15%) gas was used throughout. The tellurene flakes were obtained on the top surface and identified via optical microscope.

4.3. Characterization

The PVD-grown tellurene flakes in free standing form were characterized using high angle annular dark-field scanning transmission electron microscopy (HAADF-STEM) & HRTEM imaging on a double aberration-corrected FEI Titan Themis³ S/TEM and JEOL JEM-2100F FEG-TEM operating at 80 kV and 300 kV respectively. Samples for TEM were transferred via standard PMMA-mediated process involving spin-coating of the polymer on as-grown substrate and etching underlying SiO_2 layer with 2M KOH, followed by rinsing the 'polymer+sample' film in DI water before scooping up on a holey carbon grid (Ted Pella). The grid was cleaned in acetone & IPA and heated overnight in a vacuum oven to minimize residual carbon contamination before imaging. PLD samples for TEM were prepared by conventional cross-sectional specimen preparation methods. The sample was bonded using 353ND epoxy (Epoxy Technology), cleaved to a $3 \text{ mm} \times 3 \text{ mm}$ piece, polished to a thickness of $\sim 70 \text{ } \mu\text{m}$ (Allied Multiprep), and milled to electron transparency under Ar^+ beam (Fishione Model 1010 ion mill). Images were acquired aligned to the MgO [001] zone axis. Raman spectra were obtained on a Renishaw inVia machine with a 532 nm laser focused through a $50\times$ objective. The samples for the temperature dependent Raman measurements were secured in a LinkamTM microscope stage which was sealed inside in an inert argon environment to prevent the effects of oxidation. AFM images were recorded on a Bruker Multimode 8 in tapping and quantum nano-mechanical mode.

Acknowledgments

AA, EB, and AK contributed equally. Experiments were designed by AA, EB, ER, CST, VK, & PMA. Sample growth and AFM analysis was done by AA & EB. VK, RR, AA, & EB performed Raman spectroscopy. S/TEM imaging & analysis was done by EB, VK, CST, & SY. Theoretical computations were done by AK, HK, FS, AN, RKK & PV. The manuscript was written through contributions of all authors. All authors have given approval to the final version of the manuscript. The authors declare no competing financial interest.

This work was supported as part of the Computational Materials Sciences Program funded by the US Department of Energy, Office of Science, Basic Energy Sciences, under Award Number DE-SC0014607. Elisabeth Bianco acknowledges the support of the National Science Foundation Graduate Research Fellowship under Grant No. (DGE-1450681). This work was supported by the Nanoelectronics Branch, Functional Materials Division, Materials and Manufacturing Directorate, Air Force Research Laboratory. Emilie Ringe acknowledges Air Force Office of Scientific Research Grant No. AFOSR-YIP FA9550-17-1-0202. The authors acknowledge Dr Krishnamurthy Mahalingam and the Materials Characterization Facility in the Materials and Manufacturing Directorate, Air Force Research Laboratory for their contributions to the electron microscopy.

ORCID iDs

Amey Apte  <https://orcid.org/0000-0001-6337-5406>

Elisabeth Bianco  <https://orcid.org/0000-0003-3211-9375>

Aravind Krishnamoorthy  <https://orcid.org/0000-0001-6778-2471>

Nicholas Glavin  <https://orcid.org/0000-0002-9447-7509>

Vikas Varshney  <https://orcid.org/0000-0002-2613-458X>

Emilie Ringe  <https://orcid.org/0000-0003-3743-9204>

Aiichiro Nakano  <https://orcid.org/0000-0003-3228-3896>

Chandra Sekhar Tiwary  <https://orcid.org/0000-0001-9760-9768>

References

- [1] Novoselov K S, Geim A K, Morozov S V, Jiang D, Katsnelson M I, Grigorieva I V, Dubonos S V and Firsov A A 2005 Two-dimensional gas of massless Dirac fermions in graphene *Nature* **438** 197–200
- [2] Geim A K and Novoselov K S 2007 The rise of graphene *Nat. Mater.* **6** 183–91
- [3] Geim A K 2009 Graphene: status and prospects *Science* **324** 1530–4
- [4] Novoselov K S, Jiang D, Schedin F, Booth T J, Khotkevich V V, Morozov S V and Geim A K 2005 Two-dimensional atomic crystals *Proc. Natl Acad. Sci. USA* **102** 10451–3

- [5] Geim A K and Grigorieva I V 2013 Van der Waals heterostructures *Nature* **499** 419–25
- [6] Mak K F, Lee C, Hone J, Shan J and Heinz T F 2010 Atomically thin MoS₂: a new direct-gap semiconductor *Phys. Rev. Lett.* **105** 136805
- [7] Liu D et al 2012 Electronic origin of high-temperature superconductivity in single-layer FeSe superconductor *Nat. Commun.* **3** 931
- [8] Qing-Yan W et al 2012 Interface-induced high-temperature superconductivity in single unit-cell FeSe films on SrTiO₃ *Chin. Phys. Lett.* **29** 37402
- [9] Wu M K, Ashburn J R, Torng C J, Hor P H, Meng R L, Gao L, Huang Z J, Wang Y Q and Chu C W 1987 Superconductivity at 93 K in a new mixed-phase Y–Ba–Cu–O compound system at ambient pressure *Phys. Rev. Lett.* **58** 908–10
- [10] Ni Z, Liu Q, Tang K, Zheng J, Zhou J, Qin R, Gao Z, Yu D and Lu J 2012 Tunable bandgap in silicene and germanene *Nano Lett.* **12** 113–8
- [11] Mannix A J et al 2015 Synthesis of borophenes: Anisotropic, two-dimensional boron polymorphs *Science* **350** 1513–6
- [12] Zhu F, Chen W, Xu Y, Gao C, Guan D, Liu C, Qian D, Zhang S-C and Jia J 2015 Epitaxial growth of two-dimensional stanene *Nat. Mater.* **14** 1020–5
- [13] Liu H, Neal A T, Zhu Z, Luo Z, Xu X, Tománek D and Ye P D 2014 Phosphorene: an unexplored 2D semiconductor with a high hole mobility *ACS Nano* **8** 4033–41
- [14] Bianco E, Butler S, Jiang S, Restrepo O D, Windl W and Goldberger J E 2013 Stability and exfoliation of germanane: a germanium graphane analogue *ACS Nano* **7** 4414–21
- [15] Britnell L et al 2012 Electron tunneling through ultrathin boron nitride crystalline barriers *Nano Lett.* **12** 1707–10
- [16] Kane C L and Mele E J 2005 Quantum spin Hall effect in graphene *Phys. Rev. Lett.* **95** 226801
- [17] Liu C C, Feng W and Yao Y 2011 Quantum spin Hall effect in silicene and two-dimensional germanium *Phys. Rev. Lett.* **107** 076802
- [18] Molle A, Goldberger J, Houssa M, Xu Y, Zhang S-C and Akinwande D 2017 Buckled two-dimensional Xene sheets *Nat. Mater.* **16** 163–9
- [19] Li L, Yu Y, Ye G J, Ge Q, Ou X, Wu H, Feng D, Chen X H and Zhang Y 2014 Black phosphorus field-effect transistors *Nat. Nanotechnol.* **9** 372–7
- [20] Koenig S P, Doganov R A, Schmidt H, Castro Neto A H and Özyilmaz B 2014 Electric field effect in ultrathin black phosphorus *Appl. Phys. Lett.* **104** 103106
- [21] Carvalho A, Wang M, Zhu X, Rodin A S, Su H and Castro Neto A H 2016 Phosphorene: from theory to applications *Nat. Rev. Mater.* **1** 16061
- [22] Feng B, Zhang J, Zhong Q, Li W, Li S, Li H, Cheng P, Meng S, Chen L and Wu K 2016 Experimental realization of two-dimensional boron sheets *Nat. Chem.* **8** 563–8
- [23] Wang Q, Safdar M, Xu K, Mirza M, Wang Z and He J 2014 Van der Waals epitaxy and photoresponse of hexagonal tellurium nanoplates on flexible mica sheets *ACS Nano* **8** 7497–505
- [24] Kresse G, Furthmüller J and Hafner J 1994 Theory of the crystal structures of selenium and tellurium: the effect of generalized-gradient corrections to the local-density approximation *Phys. Rev. B* **50** 13181–5
- [25] Hirayama M, Okugawa R, Ishibashi S, Murakami S and Miyake T 2015 Weyl node and spin texture in trigonal tellurium and selenium *Phys. Rev. Lett.* **114** 1–8
- [26] Nakayama K, Kuno M, Yamauchi K, Souma S, Sugawara K, Oguchi T, Sato T and Takahashi T 2017 Band splitting and Weyl nodes in trigonal tellurium studied by angle-resolved photoemission spectroscopy and density functional theory *Phys. Rev. B* **95** 125204
- [27] Liu P, Ma Y, Cai W, Wang Z, Wang J, Qi L and Chen D 2007 Photoconductivity of single-crystalline selenium nanotubes *Nanotechnology* **18** 205704
- [28] Safdar M and Zhan X, Niu M, Mirza M, Zhao Q, Wang Z, Zhang J, Sun L and He J 2013 Site-specific nucleation and controlled growth of a vertical tellurium nanowire array for high performance field emitters *Nanotechnology* **24** 185705
- [29] Wang Q, Safdar M, Wang Z and He J 2013 Low-dimensional Te-based nanostructures *Adv. Mater.* **25** 3915–21
- [30] Xia Y, Yang P, Sun Y, Wu Y, Mayers B, Gates B, Yin Y, Kim F and Yan H 2003 One-dimensional nanostructures: synthesis, characterization, and applications *Adv. Mater.* **15** 353–89
- [31] Wang Q, Safdar M, Zhan X and He J 2013 Controllable wettability by tailoring one-dimensional tellurium micro-nanostructures *CrystEngComm* **15** 8475–82
- [32] Gao Z, Tao F and Ren J 2018 Unusually low thermal conductivity of atomically thin 2D tellurium *Nanoscale* **10** 12997–13003
- [33] Xian L, Perez Paz A, Bianco E, Ajayan P and Rubio A 2017 Square selenene and tellurene: novel group VI elemental 2D materials with nontrivial topological properties *2D Mater.* **4** 41003
- [34] Wu B, Liu X, Yin J and Lee H 2017 Bulk β -Te to few layered β -tellurenes: indirect to direct band-gap transitions showing semiconducting property *Mater. Res. Express* **4** 95902
- [35] Qiao J, Pan Y, Yang F, Wang C, Chai Y and Ji W 2018 Few-layer tellurium: one-dimensional-like layered elementary semiconductor with striking physical properties *Sci. Bull.* **63** 159–68
- [36] Wang C, Qiao J, Pan Y, Zhou L, Kong X and Cheng Z 2018 Charge tunable structural phase transitions in few-layer tellurium: a step toward building mono-elemental devices (arXiv:1806.06550)
- [37] Zhu Z et al 2017 Multivalency-driven formation of Te-based monolayer materials: a combined first-principles and experimental study *Phys. Rev. Lett.* **119** 106101
- [38] Du Y, Qiu G, Wang Y, Si M, Xu X, Wu W and Ye P D 2017 One-dimensional van der Waals material tellurium: raman spectroscopy under strain and magneto-transport *Nano Lett.* **17** 3965–73
- [39] Wang Y et al 2018 Field-effect transistors made from solution-grown two-dimensional tellurene *Nat. Electron.* **1** 228–36
- [40] Huang X, Guan J, Lin Z, Liu B, Xing S, Wang W and Guo J 2017 Epitaxial growth and band structure of Te film on graphene *Nano Lett.* **17** 4619–23
- [41] Capers M J and White M 1971 Structure, growth and orientation of vacuum deposited tellurium films *Thin Solid Films* **8** 317–31
- [42] Weidmann E J and Anderson J C 1971 Structure and growth of oriented tellurium thin films *Thin Solid Films* **7** 265–76
- [43] Brooks L S 1952 The vapor pressures of tellurium and selenium *J. Am. Chem. Soc.* **74** 227–9
- [44] Ubelis A P 1982 Temperature dependence of the saturated vapor pressure of tellurium *J. Eng. Phys.* **42** 309–15
- [45] Cullity B D and Stock S R 1978 Appendix 5 *Elements of X-ray Diffraction* 2nd edn (Boston, MA: Addison-Wesley) p 507
- [46] Bangert U, Gass M H, Bleloch A L, Nair R R and Geim A K 2009 Manifestation of ripples in free-standing graphene in lattice images obtained in an aberration-corrected scanning transmission electron microscope *Phys. Status Solidi* **206** 1117–22
- [47] Brivio J, Alexander D T L and Kis A 2011 Ripples and layers in ultrathin MoS₂ membranes *Nano Lett.* **11** 5148–53
- [48] Wang W L, Bhandari S, Yi W, Bell D C, Westervelt R and Kaxiras E 2012 Direct imaging of atomic-scale ripples in few-layer graphene *Nano Lett.* **12** 2278–82
- [49] Bertolazzi S, Brivio J and Kis A 2011 Stretching and breaking of ultrathin MoS₂ *ACS Nano* **5** 9703–9
- [50] Şahin H, Cahangirov S, Topsakal M, Bekaroglu E, Akturk E, Senger R T and Ciraci S 2009 Monolayer honeycomb structures of group-IV elements and III–V binary compounds: first-principles calculations *Phys. Rev. B* **80** 155453

- [51] Zhao J *et al* 2016 Rise of silicene: a competitive 2D material *Prog. Mater. Sci.* **83** 24–151
- [52] Jiang J-W and Park H S 2014 Mechanical properties of single-layer black phosphorus *J. Phys. D: Appl. Phys.* **47** 385304
- [53] Martin R M, Lucovsky G and Helliwell K 1976 Intermolecular bonding and lattice dynamics of Se and Te *Phys. Rev. B* **13** 1383–95
- [54] Boulard B, Kieffer J, Phifer C C and Angell C A 1992 Vibrational spectra in fluoride crystals and glasses at normal and high pressures by computer simulation *J. Non-Cryst. Solids* **140** 350–8
- [55] Yan Z, Jiang C, Pope T R, Tsang C F, Stickney J L, Goli P, Renteria J, Salguero T T and Balandin A A 2013 Phonon and thermal properties of exfoliated TaSe₂ thin films *J. Appl. Phys.* **114** 204301
- [56] Taube A, Judek J, Jastrzębski C, Dużyńska A, Świtkowski K and Zdrojek M 2014 Temperature-dependent nonlinear phonon shifts in a supported MoS₂ monolayer *ACS Appl. Mater. Interfaces* **6** 8959–63